Deep Learning Accelerated Quantum Transport Simulations in Nanoelectronics: From Break Junctions to Field-Effect Transistors

Jijie Zou [2,3], Zhanghao Zhouyin,[2, 4] Dongying Lin,[5] Linfeng Zhang,[2, 6] Shimin Hou,[3, 5, *] and Qiangqiang Gu[1, 2, 7, †]

[1]*School of Artificial Intelligence and Data Science,*
University of Science and Technology of China, Hefei 230026, China
[2]*AI for Science Institute, Beijing 100080, China*
[3]*Centre for Nanoscale Science and Technology, Academy for Advanced*
Interdisciplinary Studies, Peking University, Beijing 100871, China
[4]*Department of Physics, McGill University, Montreal, Quebec, Canada H3A2T8*
[5]*Key Laboratory for the Physics and Chemistry of Nanodevices,*
School of Electronics, Peking University, Beijing 100871, China
[6]*DP Technology, Beijing 100080, China*
[7]*Suzhou Institute for Advanced Research,*
University of Science and Technology of China, Suzhou 215123, China

Quantum transport simulations are essential for understanding and designing nanoelectronic devices, yet the longstanding trade-off between accuracy and computational efficiency has limited their practical applications. We present a general integrated framework that combines the deep learning tight-binding Hamiltonian (DeePTB) approach with the non-equilibrium Green's Function (NEGF) method, enabling efficient quantum transport calculations with first-principles accuracy. The capabilities of the DeePTB-NEGF framework are demonstrated through two representative applications: comprehensive simulation of break junction systems, where conductance histograms exhibit good agreement with experimental measurements in both metallic contact and single-molecule junction cases; and simulation of carbon nanotube field-effect transistors in the experimental dimensions using NEGF-Poisson self-consistency, achieving excellent alignment with measured transfer characteristics. Furthermore, our simulation reveals the limited scaling down potential for local bottom gate geometry into sub-5 nm due to performance degradation. By bridging the gap between first-principles accuracy and computational efficiency, our framework provides a powerful tool for high-throughput quantum transport simulations across different scales in nanoelectronics.

I. INTRODUCTION

Quantum transport simulations are essential for understanding and designing nanoelectronic devices. The non-equilibrium Green's function (NEGF) method[1–3], combined with density functional theory (DFT)[4, 5], has established itself as the standard approach for investigating quantum transport phenomena at the first-principles level[6, 7]. However, the computational burden of DFT-NEGF self-consistent field (SCF) iterations severely constrains its practical applications, which is particularly critical in studying large-scale systems and dynamic processes. This limitation is especially critical in scenarios such as break junction experiments [8, 9], where thousands of conductance measurements are required for statistical analysis, and in simulating field-effect transistors (FETs) with experimentally realistic dimensions. In both cases, the extensive computational resources required make first-principles calculations prohibitively expensive, often restricting studies to selected configurations or significantly downsized systems. This compromise between computational feasibility and experimental relevance highlights the urgent need for more efficient approaches that can maintain first-principles ac-

curacy while dramatically reducing computational costs.

Machine learning (ML) approaches have emerged as promising alternatives to accelerate quantum transport calculations. There are several ML attempts including direct prediction of conductance from atomic structures using local descriptors[10], and mapping combined structural and electronic features to transmission spectra near the Fermi level[11]. While these approaches demonstrate the potential of ML in transport calculations, they are often limited to specific systems or single transport property, lacking the generality required for broad applications in nanoelectronics. A systematic and comprehensive framework to accelerate DFT-NEGF simulations and capable of predicting various transport properties - from transmission spectra to current-voltage characteristics - remains elusive.

The key to addressing this challenge is to bypass the time-consuming DFT-NEGF SCF iterations while maintaining first-principles accuracy. Our recently developed deep learning represented tight-binding (TB) Hamiltonian method, DeePTB[12, 13], provides an efficient route to accurate electronic structure calculations. By combining deep neural networks with physics-based principles, DeePTB achieves remarkable accuracy in predicting both local environment-dependent Slater-Koster (SK) tight-binding Hamiltonians[12] and DFT Hamiltonians, overlap and density matrix in the linear combination of atomic orbitals (LCAO) basis[13]. Building on

arXiv:2411.08800v2 [cond-mat.mes-hall] 9 Feb 2025

these capabilities, we introduce DeePTB-NEGF, a general integrated framework for efficient quantum transport calculations. This framework enables direct prediction of TB models or DFT Hamiltonians as well as the overlap matrices, eliminating the need for DFT-NEGF SCF while preserving first-principles accuracy.

We demonstrate the versatility and accuracy of our approach through two representative applications: (1) break junction systems, where we successfully simulate the dynamic process of metallic contacts and single-molecule junctions, showing good agreement with both DFT-NEGF calculations and experimental measurements[14]; and (2) carbon nanotube field-effect transistors (CNT-FETs), where we incorporate Poisson equation calculations within the DeePTB-NEGF framework to model the transport characteristics of CNT-FETs at experimental-scale dimensions under finite bias, exhibiting excellent consistency with the experimental results [15]. These applications demonstrate that our framework can efficiently handle quantum transport across different scales and materials systems, opening new possibilities for high-throughput quantum transport calculations in nanoelectronics.

II. METHODOLOGY AND WORKFLOW

Efficient first-principles quantum transport simulations require accurate electronic structure description while avoiding the computationally expensive DFT-NEGF SCF iterations. Our approach combines the NEGF formalism for transport calculations with the DeePTB method for efficient Hamiltonian prediction, as illustrated in Fig. 1. DeePTB offers two complementary strategies for constructing electronic Hamiltonians: (1) the environment-dependent SK tight-binding Hamiltonians[12] and (2) DFT Hamiltonians in the LCAO basis with E(3) equivariant graph neural networks[13].

For the SK tight-binding Hamiltonians, DeePTB trains local environment-dependent SK integrals $h_{ll'\zeta}^{\text{env}}$ as[12]:

$$h_{ll'\zeta}^{\text{env}} = h_{ll'\zeta}(r_{ij}) \times \left[1 + \Phi_{ll'\zeta}^{o_i,o_j}\left(r_{ij}, \mathcal{D}^{ij}\right)\right] \quad (1)$$

where $h_{ll'\zeta}(r_{ij})$ is the conventional SK integral, $\Phi_{ll'\zeta}^{o_i,o_j}$ introduces neural network-based environmental corrections through the descriptor $\mathcal{D}^{ij}$. Here, l, l' denote atomic orbitals, ζ the bond types, and r_{ij} the interatomic distance. By training on the DFT eigenvalues, the SK integrals as functions of the local environment can be predicted for unseen structures.

For the LCAO DFT Hamiltonians, DeePTB predicts multiple quantum operators (Hamiltonian, overlap and density matrices) through E(3) equivariant graph neural networks[13], preserving rotational symmetry through angular momentum coupling:

$$O_{l_1,l_2,m_1,m_2}^{i,j} = \sum_{l_3,m_3} C_{(l_1,m_1)(l_2,m_2)}^{(l_3,m_3)} o_{l_3,m_3}^{i,j} \quad (2)$$
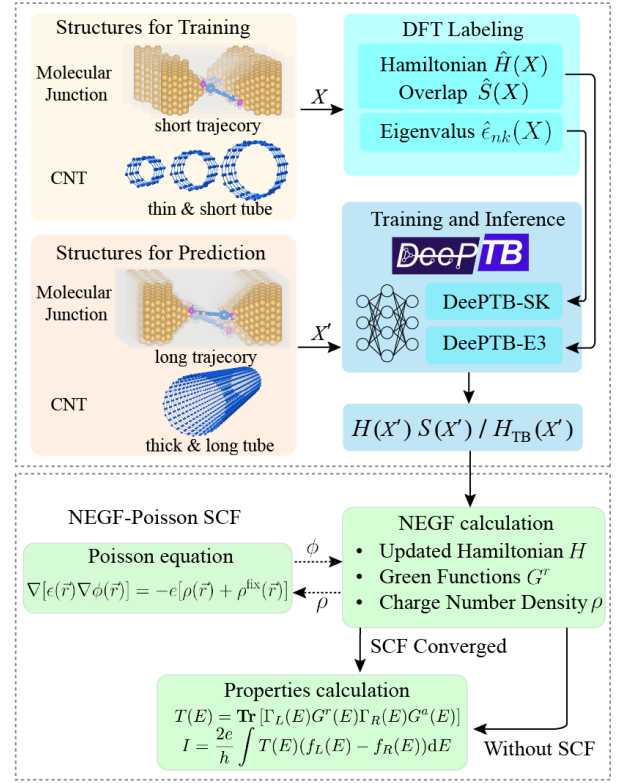

FIG. 1. Schematic illustration of DeePTB-NEGF workflow. Atomic configurations X and X' are structures for training and prediction respectively. Reference Hamiltonians/overlap matrices $\hat{H}(X)/\hat{S}(X)$ and reference eigenvalues $\hat{\epsilon}_{nk}(X)$ are obtained from first-principles calculations, while $H(X')/ S(X')$ and $H_{\text{TB}}(X')$ represent predictions from DeePTB model with E3 method and SK method respectively. $T(E)$ denotes the transmission coefficient at energy E and I the current through the device.

where O represents the quantum operators (Hamiltonian, overlap and density matrices), $C_{(l_1,m_1)(l_2,m_2)}^{(l_3,m_3)}$ are the Clebsch-Gordan coefficients and $o_{l_3,m_3}^{i,j}$ are the output node or edge features from the equivariant graph neural networks. Both strategies provide efficient access to electronic Hamiltonians while maintaining first-principles accuracy, though based on different theoretical frameworks.

With the Hamiltonians efficiently predicted by DeePTB, quantum transport properties are calculated using the NEGF formalism. The NEGF approach provides a rigorous framework for quantum transport by incorporating open boundary conditions through self-energies $\mathbf{\Sigma}$ that describe the coupling between the device and semi-infinite electrodes. For a two-terminal system, the transmission spectrum $T(E)$ between the left and right electrodes is given by:

$$T(E) = \mathbf{Tr}\left[\Gamma_L(E)G^r(E)\Gamma_R(E)G^a(E)\right] \quad (3)$$

where $\Gamma_{L/R} = i(\mathbf{\Sigma}_{L/R}^r - \mathbf{\Sigma}_{L/R}^a)$ is the broadening function for the left (L) and right (R) electrodes and $G^{r/a}(E) =$

$[(E \pm i\eta)S - H - \mathbf{\Sigma}_L^{r/a} - \mathbf{\Sigma}_R^{r/a}]^{-1}$ is the retarded/advanced Green's function with η being a positive infinitesimal and H/S being the Hamiltonian/overlap matrices. The current (I) and zero-bias conductance (G) at the zero-temperature limit are then given by[8]:

$$I = \frac{2e}{h} \int T(E)(f_L(E) - f_R(E))\mathrm{d}E \qquad (4)$$

$$G = \frac{2e^2}{h} T(E_f) = T(E_f)\mathrm{G}_0 \qquad (5)$$

where $f_{L/R}(E)$ are Fermi-Dirac distributions for the left and right electrodes, E_f is the Fermi energy, $\mathrm{G}_0 = 2e^2/h$ is the quantum conductance, e is the elementary charge, and h is the Planck's constant.

Building upon the efficient Hamiltonian prediction by DeePTB, we further optimize the NEGF calculations through addressing its two most time-consuming operations: the calculation of electrode self-energies and matrix inversion for Green's functions. For the electrode self-energy calculations, we exploit the fact that in nanoelectronics, particularly in molecular electronics, electrodes can often be considered periodic in the directions perpendicular to the current. By applying Bloch's theorem, we calculate the self-energy within the smallest electrode unit cell[16], significantly reducing both memory requirements and computational costs. For the Green's function calculations, we utilize the sparse nature of the Hamiltonian and overlap matrices in the local basis representation, which leads to block tridiagonal matrix configurations in quasi-one-dimensional systems[17]. We implement a greedy algorithm with recursive processing[18] to optimize the matrix structure, which substantially enhances the efficiency of the recursive Green's function calculations[19].

The complete workflow is illustrated in Fig. 1. The training set consists of atomic configurations labeled with converged Hamiltonians and overlap matrices $\hat{\boldsymbol{H}}(X)$ and $\hat{\boldsymbol{S}}(X)$ obtained from DFT-NEGF calculations using TranSIESTA[6, 16], or eigenvalues $\hat{\epsilon}_{\mathrm{nk}}(X)$ from DFT calculations performed with SIESTA[20]. For a new configuration X', the trained DeePTB model can efficiently predict the DFT Hamiltonians and overlap matrices $\boldsymbol{H}(X')$ and $\boldsymbol{S}(X')$, or construct tight binding Hamiltonians $\boldsymbol{H}_{\mathrm{TB}}(X')$, enabling high-throughput quantum transport calculations through the optimized NEGF framework. Furthermore, the DeePTB-NEGF framework extends to quantum transport simulations in devices under finite bias via NEGF-Poisson SCF iterations, as detailed in Section III B.

III. RESULTS

A. Break Junction Systems

Break junction experiments, primarily implemented through mechanically controllable break junctions or scanning tunneling microscopy break junctions[8, 9], provide a powerful platform for investigating quantum transport at the atomic and molecular scales. During a typical break junction process, the configuration evolves from the metallic contacts to the molecular junctions. In the metallic contacts, conductance exhibits characteristic quantization features reflecting the discrete nature of atomic contacts. As the junction breaks, individual molecules can bridge the nanoscale gap forming a stable molecular junction[21]. Statistical analysis of these transport features requires thousands of conductance measurements over repeated breaking events, making first-principles calculations computationally prohibitive. The DeePTB-NEGF framework developed here enables efficient simulation of the break junction process while maintaining the first-principles accuracy. Below we demonstrate its capabilities in the two cases of metallic contacts and molecular junctions, providing direct comparison with experimental measurements and atomic-level insights into the quantum transport mechanisms.

1. Quantum Transport in Metallic Contacts

Gold atomic contacts formed in break junction experiments exhibit distinct quantum transport features such as conductance quantization and ballistic transport[22]. During electrode separation, the conductance evolution reveals characteristic plateaus, reflecting the formation of atomic-scale contact configurations[23]. Understanding these quantum transport features requires statistical analysis over thousands of breaking events, making theoretical reproduction of conductance histograms at the first-principles level computationally challenging.

To simulate quantum transport through gold contacts, we construct a junction model consisting of a central scattering region connected to two semi-infinite electrodes, as shown in the top panel of Fig. 2(a). The scattering region contains 304 gold atoms arranged along the [100] direction, with two bulk-like sections (100 atoms each in $5 \times 5 \times 4$ supercells) serving as electrode extensions. To simulate the break junction formation, we performed molecular dynamics simulations using the DeePMD potential[24] at 150K in the NVT ensemble, with the simulation box being the scattering region under periodic boundary conditions. During elongation, the electrode sections maintain their bulk structure while moving in opposite directions, with stretching speeds ranging from 0.2 to 5.0 m/s in each side. The structural evolution exhibits characteristic bipyramidal shapes consistent with experimental observations of gold contacts by high-resolution transmission electron microscopy [25].

For constructing the DeePTB model for gold contacts, we randomly sampled 122 configurations from 4 independent trajectories at $v = \pm 5$ m/s and calculated their electronic Hamiltonians and overlaps using DFT-NEGF with generalized gradient approximation (GGA) within the Perdew-Burke-Ernzerhof (PBE) formulation
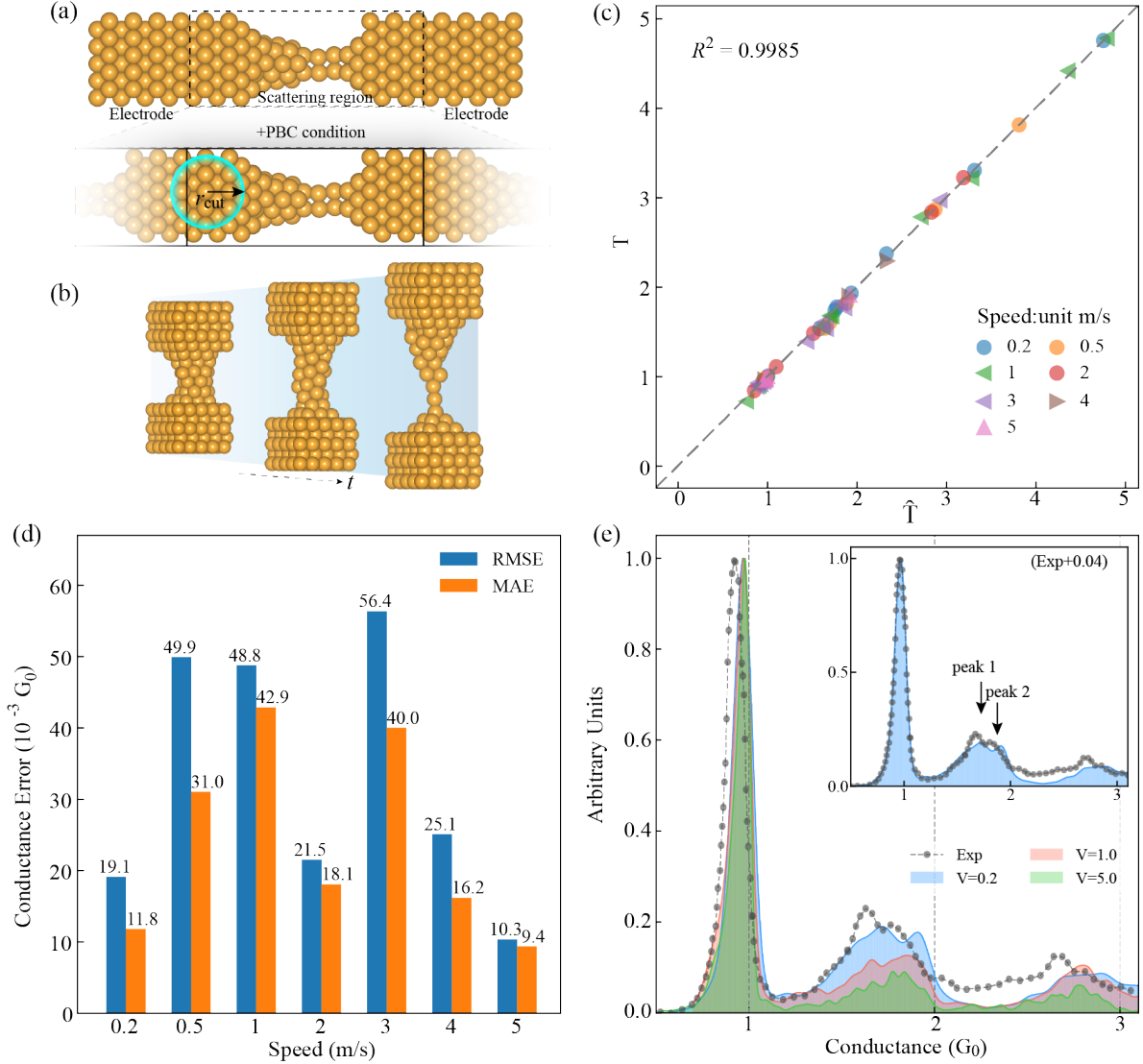
FIG. 2. DeePTB-NEGF simulation results for gold contacts. (a) Atomic configuration of gold contacts. Top panel: configuration used for transport calculation consisting of a central scattering region connected to two semi-infinite electrodes. Bottom panel: configuration used for DeePTB model training with periodic boundary conditions (PBC). The local environment inside the cutoff radius for the atoms near the simulation box edges is bulk-like. (b) Three representative snapshots in one breaking junction process. (c) Comparison for transmission at the Fermi level between the DeePTB-NEGF method (T) and DFT-NEGF calculations($\hat{T}$) in structures obtained with different elongation speeds. (d) RMSE and MAE for zero-bias conductance between DeePTB-NEGF and DFT-NEGF results. (e) Conductance histograms from DeePTB-NEGF simulations at different elongation speeds ($v = 0.2$, 1.0, and 5.0 m/s) compared with experimental data. 9224 configurations are analyzed in total. Inset: Experimental $1G_0$ peak aligns with the $v = 0.2$ m/s case after shifting the experimental histogram by $+0.04G_0$.

as exchange-correlation functional and single-zeta plus polarization(SZP) basis. The model's cutoff radius for the local environment of gold atom r_{cut}^{Au} was set to 7.4Å to match the maximum radius of gold atomic orbitals in DFT-NEGF calculations. Although the training configurations only include the scattering region, periodic boundary conditions utilized in DeePTB ensure that atoms near the simulation box edges experience a bulk-like environment within the cutoff radius, crucial for accurate self-energy calculations in the NEGF

framework. As shown in the lower panel of Fig. 2(a) and supplementary materials (SM) Fig. S1, in regions at simulation box edge (far from the structure interface), the electronic Hamiltonian matches that of bulk gold with identical local environments, differing only by a constant shift due to long-range effects. We validated this phenomenon by comparing DeePTB-predicted and DFT-calculated Hamiltonians and overlap matrices for edge atom with its bulk counterpart. The results confirm the expected shift and demonstrate the model's accuracy

for electrodes. More details of data preparation, model training and validation of model in bulk-like environment are available in SM Sec.S1.A.

We then validate the model's predictive capability for electronic properties in complete gold atomic contacts, as shown in the top panel of Fig. 2(a). Building on its accuracy in bulk-like environment, the model successfully predicts Hamiltonian for the complete atomic contact including additional electrode layers, exhibiting excellent agreement with DFT results (Hamiltonian RMSE = 7.57×10^{-4} eV for configurations in validation set, see SM Sec.S1.A for details). More importantly, we assess the model's generalization ability across different elongation speeds. Although trained exclusively on configurations from trajectories with $v = 5.0$ m/s, the model demonstrates outstanding transferability. By analyzing 55 randomly selected configurations spanning speeds from 0.2 m/s to 5.0 m/s, we compare zero-bias conductances predicted by DeePTB-NEGF with DFT-NEGF results. The model achieves exceptional accuracy with $R^2 = 0.9985$ in the parity plot and maintains low prediction errors (conductance RMSE and MAE < $60 \times 10^{-3} G_0$) across all elongation speeds, as shown in Fig. 2(c) and (d).

Having validated the model's accuracy, we then applied the model to calculate the gold contact conductance and demonstrate its efficiency in high-throughput calculations. Using the DeePTB model trained only on 122 configurations randomly sampled from 4 breaking junction trajectories, we successfully generated conductance histograms by analyzing 9224 configurations randomly sampled from 105 elongation processes at speeds of 0.2, 1.0, and 5.0 m/s. The calculations were accelerated using the Bloch theorem for self-energy evaluation and exploiting the tridiagonal block structure of Hamiltonian matrices. The histograms, normalized to their respective $1G_0$ peaks, are presented in Fig.2(e). The prominent peak at $1G_0$ corresponds to monatomic chains, a well-established signature in metallic break junctions.

Different elongation speeds lead to distinct variations in conductance peak shapes, particularly in the range from $1G_0$ to $2G_0$. This variation arises from the suppression of collective atomic relaxations at higher elongation speeds, which prolongs the stability of monatomic chains before breaking[10, 26]. Consequently, the relative intensity of conductance features beyond $1G_0$ is systematically reduced in the normalized histograms. Note that the simulation speeds (0.2-5.0 m/s) are necessarily higher than experimental rates (10 pm/s to 100 nm/s)[8], because the experimental breaking processes would require prohibitively large MD simulation times[25]. Nevertheless, even at these elevated speeds, our simulated conductance histogram at $v = 0.2$ m/s shows good agreement with experimental measurements, despite small shifts in peak positions. These shifts can be attributed to the fixed perfect lattice structure imposed on the electrode boundary atoms in the simulation, which neglects the experimental structural perturbation and minor defects.

By shifting the experimental histogram by $+0.04 G_0$, we achieve excellent shape alignment of the $1G_0$ peaks as shown in the inset of Fig. 2(e). The aligned histograms reveal remarkable agreement between calculation and experiment [25], particularly in reproducing two characteristic conductance peaks between $1G_0$ and $2G_0$. These results demonstrate that our DeePTB-NEGF framework can efficiently and accurately predict the quantum transport properties of gold contacts, capturing the statistical features of the conductance histograms consistent with the experimentally observed characteristics.

2. Quantum Transport through Single-molecule Junctions

Single-molecule junctions present additional challenges for quantum transport calculations compared to metallic contacts due to their complex chemical environments and dynamic metal-molecule interfaces. Their transmission spectra are particularly sensitive to molecular conformations and contact geometries, requiring extensive sampling to capture the dynamic features during junction formation and breaking in the break junction experiments. While DFT-NEGF calculations can accurately predict transmission spectra for static configurations, their computational cost has restricted most studies to selected relaxed structures, missing crucial dynamic aspects of the transport process. We demonstrate that our DeePTB-NEGF framework efficiently addresses this challenge by enabling high-throughput transmission spectra calculations throughout the entire junction evolution.

The molecule investigated here is a classical π-conjugated system with sulfur methyl as anchoring groups, which contains rich chemical environments and flexible configurations due to three types of carbon bonds and the dihedral angle between the two benzene planes (top left inset of Fig. 3(c)). The scattering region consists of the molecule connected to gold electrodes with a bi-pyramidal shape, where each electrode principal layer contains 144 atoms ($6 \times 6 \times 4$ supercell). To simulate the breaking junction process, we performed MD simulations at 300K using the ReaxFF reactive force field[27], which can efficiently describe chemical bonding through its empirical bond-order formalism. During stretching, the gold electrodes move in opposite directions at a speed of $v = \pm 2$ m/s, with three representative snapshots at t_1, t_2, t_3 in equal time intervals shown in Fig. 3(a). To construct the DeePTB model for molecular junctions, we randomly sampled 268 configurations from 14 breaking junction trajectories as the training set and calculated their electronic Hamiltonians and overlaps using DFT-NEGF with PBE functional and SZP basis in TranSI-ESTA. Similarly, the model's cutoff radius was set as the largest radius of atomic orbitals for each element in DFT-NEGF calculations, ensuring accurate description of electronic interactions. More details of data preparation and model training are provided in the SM Sec.S1.B.

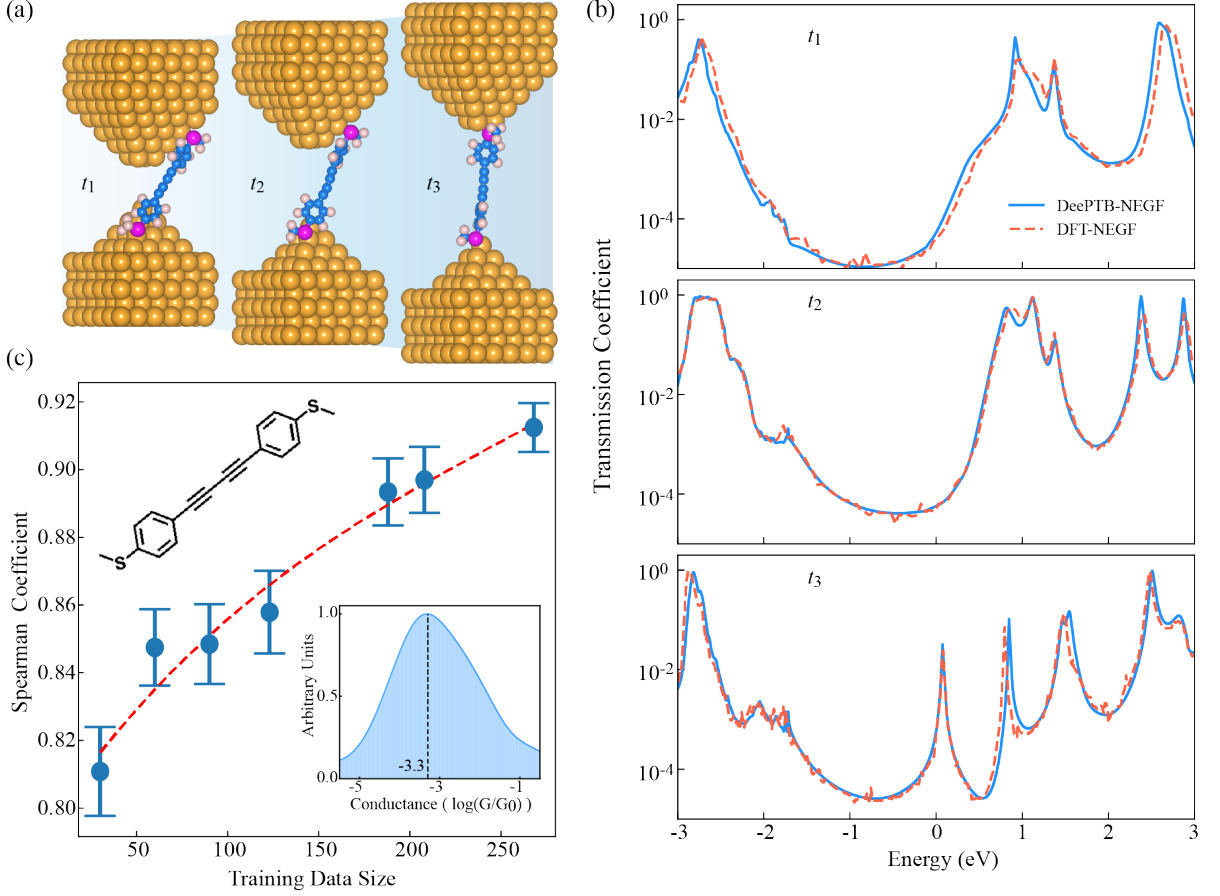To understand how the training set size affects model

FIG. 3. DeePTB-NEGF simulation results for molecular junctions. (a) Three sequential snapshots of the molecular junction breaking process at equal time intervals (t_1, t_2, and t_3). (b) Transmission spectra corresponding to the three snapshots in (a). (c) Spearman correlation coefficient of transmission spectra calculated for validation set configurations across varying training data sizes, within the energy range of -0.5 to 0.5 eV. Blue dots represent mean values with error bars showing standard deviations. Top left inset: Molecular structure in the junction. Bottom right inset: Conductance histogram computed from 590 configurations across 11 stretching processes using DeePTB-NEGF, showing the highest peak at $10^{-3.3}G_0$.

performance, we trained a series of models using varying numbers of configurations (30, 60, 90, 123, 188, 208, 268) randomly sampled from the 14 breaking junction trajectories. The prediction accuracy was evaluated using the Spearman correlation coefficient between DeePTB-NEGF and DFT-NEGF transmission spectra, which measures how well two variables can be described by a monotonic function[28]. The coefficients are evaluated in the energy range of -0.5 to 0.5 eV with a step of 0.01 eV, utilizing a validation set of 60 configurations from different trajectories to test out-of-distribution generalization. As shown in Fig. 3(c), both the mean value and standard deviation of the correlation coefficient improve with increasing training set size, reaching a high correlation of 0.912 with 268 configurations. The gradually reduced improvement rate suggests that our model has achieved sufficient accuracy in capturing the structural complexity present in the breaking junction process.

To further validate the statistical assessment of model accuracy indicated by the Spearman correlation coeffi-

cient of 0.912, we examine the performance of our model trained with 268 configurations by comparing transmission spectra for three representative configurations captured at times t_1, t_2, and t_3 during the breaking junction process shown in Fig.3(a). As illustrated in Fig.3(b), the DeePTB-NEGF predicted transmission spectra closely match the DFT-NEGF results across different junction configurations, accurately reproducing both the positions and heights of transmission peaks. Analysis of these transmission spectra further reveals distinct behavior of frontier molecular orbital contributions: the HOMO-dominated transmission peak maintains its energetic position relative to the Fermi level, while the LUMO-dominated peak shifts toward the Fermi level during junction elongation. This characteristic evolution of transmission peaks indicates that the conductance is LUMO-dominated, which is consistent with previous experimental and theoretical studies[14]. Furthermore, to enable statistical comparison with experimental measurements, we calculated the zero-bias conductance for

590 configurations sampled from 11 breaking junction trajectories. The resulting conductance histogram (bottom right inset of Fig. 3(c)) shows a pronounced peak at $10^{-3.3}G_0$, in good agreement with the experimental value of $10^{-3.6}G_0$[14].

In summary, we have demonstrated the applicability and accuracy of the DeePTB-NEGF approach in simulating quantum transport properties in the two cases of metallic atomic contacts and single-molecule junctions. Our method successfully captures the key features of the conductance evolution during the junction-breaking process and reproduces the main characteristics of the experimental conductance histograms. The good agreement between the DeePTB-NEGF and DFT-NEGF results further validates its accuracy in describing the electronic structure of the junctions. These results establish DeePTB-NEGF as a powerful and efficient method for studying quantum transport in break junction systems, bridging the gap between first-principles accuracy and statistical analysis.

B. Carbon Nanotube Field-effect Transistor

Having demonstrated the capability of DeePTB-NEGF in simulating quantum transport in break junction systems, we now extend this framework to field-effect transistors (FETs). The critical distinction in FETs is the presence of gate-modulated electrostatics, which necessitates a self-consistent solution of the Poisson equation coupled with the NEGF formalism [29, 30]. This extension enables the simulation of more complex nanoelectronic devices where the interplay between quantum transport and electrostatic effects is paramount. We apply this enhanced methodology to carbon nanotube field-effect transistors (CNT-FETs), which are promising candidates for next-generation electronics due to their exceptional charge transport properties [31–33]. The quasi-one-dimensional structure and long mean free path of CNTs facilitate near-ballistic transport at nanoscale dimensions, making them ideal for high-performance devices [34]. Accurate modeling of CNT-FETs requires capturing the gate-voltage-dependent modulation of carrier transport, a challenge well-suited to our extended DeePTB-NEGF approach.

To incorporate gate electrostatics in CNT-FET simulations, we implement the NEGF-Poisson formalism using TB models predicted by DeePTB, which provides local environment-dependent corrections to the Slater-Koster parameters (Eq. 1), offering advantages over DFT Hamiltonian models due to their smaller, sparser matrices and direct compatibility with the NEGF-Poisson framework. This self-consistency is achieved through the Gummel iteration scheme [35], which begins with the equilibrium TB Hamiltonian H_0 and iteratively solves for the non-equilibrium potential profile using the Poisson equation [36, 37]

$$\nabla[\epsilon(\vec{r})\nabla\phi_{n+1}(\vec{r})] = -e[\rho_n(\vec{r}) + \rho^{fix}(\vec{r})]. \qquad (6)$$

with the Newton-Raphson method on a discrete real-space grid. Here ϵ is the dielectric constant, ϕ_{n+1} and ρ_n are the electrostatic potential and free charge number concentration in the n-th iteration. The term ρ^{fix} represents the average equivalent charge associated with ionized donors or acceptors at each atomic site within the doped region. In practical calculations, ρ_n is obtained as Mulliken charge at all atomic sites based on the Hamiltonian H_n from the n-th iteration . The boundary conditions for the Poisson equation include constraints from gate voltage V_{gs} and drain-source bias V_{ds}. Within DeePTB-NEGF framework, the predicted TB Hamiltonian is updated according to the electrostatic potential as:

$$H_n^i = H_0^i - e\phi_n(\vec{r}_i) \qquad (7)$$

where H_n^i and $\phi_n(\vec{r}_i)$ are the n-th iteration Hamiltonian onsite block and electrostatic potential at site i, respectively. The complete NEGF-Poisson procedure is detailed in Sec.S2.B in SM. Our implementation has been validated against the established TB-NEGF code NanoTCAD ViDES [36, 38], as described in SM Sec.S2.C.

We now apply the DeePTB-NEGF framework to study the transport properties of a local bottom gate (LBG) CNT-FET with experimental dimensions, demonstrating the capability of our method to simulate realistic nanoelectronic devices that are challenging for traditional first-principles approaches due to their large size. The LBG CNT-FET geometry, shown in Fig. 4(a), has been experimentally realized with sub-10 nm channel lengths [15]. This device exhibits remarkable performance, including an ON-OFF current ratio (I_{on}/I_{off}) of 10^4 and a subthreshold slope (SS) of 94 mV/decade for a 9 nm channel length with Pd electrodes. While numerous theoretical studies have explored the transport properties of CNT-FETs using NEGF, most are based on parameterized Hamiltonians [15, 39–41] or simulated with thinner tubes than those used in experiments due to computational limitations [42]. These approaches lack sufficient accuracy in electronic structure or direct comparability with experimental results at the first-principles level without size approximations. By simulating this specific device with DeePTB-NEGF framework, we aim to validate our method against experimental results and explore the scaling limits of CNT-FETs. This approach enables us to address challenges that are difficult for both experiments and conventional simulation techniques while avoiding inaccuracies introduced by smaller geometries when solving Poisson equation and determining charge density.

To investigate the influence of CNT diameter on device performance, we simulated CNT-FETs with various indices $(10,0), (13,0), (16,0)$ and $(17,0)$ (diameters ranging from 0.79 nm to 1.35 nm). This range encompasses the 1.3 nm diameter CNTs used in experimental devices [15], with CNT(16,0) and (17,0) (diameters 1.27 nm and 1.35 nm, respectively) being most comparable to the experimental sample. We trained a sp-TB
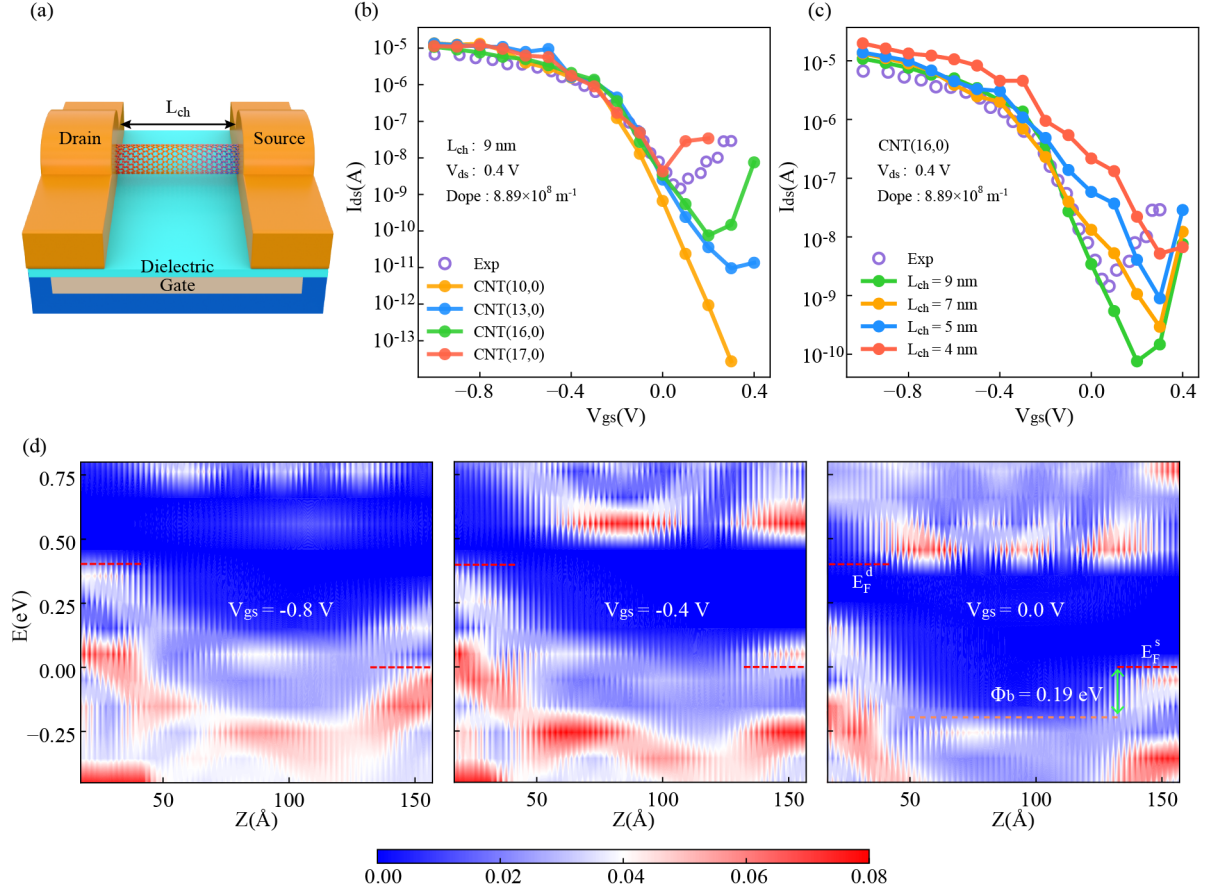
FIG. 4. DeePTB-NEGF-Poisson SCF simulation for local bottom gate carbon nanotube (LBG) field-effect transistor. (a) Schematic of the transistor geometry, where L_{ch} denotes channel length. (b)Transfer characteristics at drain-source bias $V_{ds} = 0.4$ V and dope concentrations as $8.89 \times 10^8 \mathrm{m}^{-1}$ for LBG CNT FETs using different CNT diameters. The channel length L_{ch} for all FETs are 9nm.(c)Transfer characteristics at drain-source bias $V_{ds} = 0.4$ and dope concentrations as $8.89 \times 10^8 \mathrm{m}^{-1}$ for LBG CNT FETs using different channel lengths. The tubes are all CNT(16, 0). (d) Position-resolved local density of states for CNT(17, 0) along the transport direction(z axis) with gate voltage $V_{gs} = -0.8$V, -0.4V, 0.0V. The left and right electrodes are drain and source respectively. The red dashed lines indicate the Fermi level for source and drain. The orange dashed line in $V_{gs} = 0.0$ case indicates the top of valence band inducing a barrier $\Phi_B = 0.19$ eV for holes.

model with environment-dependent SK parameter using the DFT eigenvalues of the CNT(7, 0), (10, 0), (13, 0) and (16, 0) structures as training data set, and then the band of CNT(17, 0) can be predicted. The details about data preparation and model training are provided in the SM Sec.S2.A. A comparison of band structures for these CNTs between DFT and DeePTB calculations are illustrated in the Fig. S2 in SM, validating the accuracy and generality of DeePTB model across CNTs with different diameters. To model the metal contacts, we employed a doping contact approach by setting $\rho_{fix}(r)$ in Poisson equation (Eq. 6). This method, used in previous theoretical studies [15, 42], induces a built-in electrostatic field between the doped regions and channel mimicking the band bending at the Pd electrode-CNT interface in Ohmic contacted CNT-FET [43, 44]. We tested doping concentrations ranging from $5.33 \times 10^8 \mathrm{m}^{-1}$ to $1.25 \times 10^9 \mathrm{m}^{-1}$, with results showing high consistency in

ON current and SS (see Sec. S2.D in SM). Based on these tests, we chose a doping concentration of $8.89 \times 10^8 \mathrm{m}^{-1}$ for subsequent simulations. Additionally, the bottom gate covers the channel as well as the sources and drain contacts in LBG device. Therefore, we set the total gate length as $L_{tot} = L_{ch} + 2 \times L_{ext}$, including the channel length L_{ch} and source/drain extensions L_{ext}[15]. In order to ensure the bulk-like environment inside the electrodes, different L_{ext} have been tested in Sec. S2.D in SM. It indicates that $L_{ext} = 2.5$nm is long enough to screen the impact from channel. The other detailed simulation settings are listed in Sec. S2.D in SM.

Figure 4(b) shows the simulated transfer characteristics for CNTs with different diameters, alongside experimental data. For clear comparison, the gate work functions of all devices have been shifted to have the same ON current $I_{on} \approx 1 \times 10^{-5}$ A at $V_{gs} = -1.0$ V. The numbers of atoms in these devices with 9 nm channel length are

1620, 2106, 2592 and 2754 for CNT (10,0), (13,0), (16,0) and (17,0) respectively, which are beyond the computing ability of traditional first-principles NEGF-Poisson SCF. As illustrated in Fig. 4(b), the transfer characteristics for the four tubes are similar in the ON state while becoming drastically different when entering the subthreshold region. These differences arise from the distinct band gaps of CNTs with varying diameters. For the same p-doped tube, the barrier height between the source and channel increases as the gate voltage V_{gs} becomes more positive, hindering the injection of the holes from the source. This behavior is illustrated by the local density of states (LDOS) of CNT(17, 0) shown in Fig. 4(d). Despite the differences in diameter, I_{on} remains stable at approximately 1×10^{-5} A, attributed to similar transmission functions inside the drain-source bias window in the ON state without barrier hindering (see Sec.S2.D in SM). However, the OFF current I_{off} decreases with diameter shrinkage because a larger band gap in thinner CNT tends to induce a higher potential barrier Φ_b at OFF state. The barrier suppresses source-drain tunneling, which is the major contribution to I_{off}. [40, 45]. LDOS calculations can reveal a significant decrease in Φ_b with increasing CNT diameter(see Fig. S6 in SM). At OFF states, Φ_b reduces from 0.55 eV for CNT(10,0) to 0.19 eV for CNT(17,0). Here the OFF state for CNT(10,0) is taken as $V_{gs} = 0.3$V with $I_{ds} < 10^{-13}$A. This trend is consistent with the observed increases in I_{off}. This comprehensive study of CNT diameter effects demonstrates the importance of accurately matching the simulated CNT size to experimental conditions for meaningful transfer characteristics and figures of merits such as I_{on}/I_{off}.

To investigate the scaling limit of LBG CNT-FET, we simulate the transfer characteristics using CNT(16,0) for device with various channel lengths. The scalability of FETs can be quantified by the natural length $\lambda = \sqrt{(\epsilon_{ch}/n\epsilon_{ox})t_{ox}t_{ch}}$ where n is the equivalent number of gates, ϵ_{ch} and ϵ_{ox} are the dielectric constants for channel and gate dielectric, and t_{ch} and t_{ox} represent their respective thicknesses [46]. For good electrostatics to avoid short channel effect(SCE), channel length $L_{ch} > (3 \sim 5)\lambda$ is required [33]. In LBG geometry, $\lambda \approx 0.956$nm(detialed derivation in SM Sec.S2.D). Hence we explore the geometry with channel length L_{ch} ranging from 9 nm to 4 nm, where the extent of short-channel effects (SCE) remains uncertain. As illustrated in Fig. 4(c), when L_{ch} becomes shorter the SS increases from 98.88 mV/decade to 257.27 mV/decade with I_{on}/I_{off} decreasing from 1×10^5 to 4×10^3. Obviously, it is a manifestation of SCE which can be explained by the gate electrostatic efficiency degradation in FET [33]. From the perspective of capacitance model, the gate electrostatic efficiency $\Delta V_g/\Delta\phi_{ch}$, the ability for gate voltage V_g to tune the channel potential ϕ_{ch}, can be expressed as

$$\frac{\Delta V_g}{\Delta\phi_{ch}} = 1 + \frac{C_s + C_d + C_{dep} + C_{it} + C_Q}{C_{gox'}}. \quad (8)$$

Here $C_{gox'}$ is the effective gate capacitance, C_s and C_d are parasitic capacitances from source and drain, C_{dep}, C_{it}, C_Q are capacitances induced by substrate, interface traps and mobile charge carriers respectively. With shorter channel C_s and C_d are becoming comparable to $C_{gox'}$, a result of the gate sharing control over the channel potential ϕ_{ch} with the source and drain in short-channel devices.[33]. Larger gate potential difference ΔV_g is needed to tune the same change in ϕ_{ch}, thus degrading SS. The enhancing tendency of short channel effect is also reflected by LDOS (See Fig. S7 in SM). Under identical gate and drain-source bias conditions, a shorter channel device exhibits a lower and narrower barrier, leading to substantial source-drain tunneling and an increase in I_{off} and SS [40]. Therefore, the scaling potential in the LBG geometry with a 3 nm HfO$_2$ dielectric thickness (used in our simulation and the experiment [15]) is limited, necessitating further improvements in device design. Additionally, the transfer characteristics of LBG CNT-FETs with varying channel lengths, shown in Fig. 4(c), emphasize the critical importance of simulated device dimensions in accurately reproducing the experimentally measured values, as previously discussed.

These results demonstrate the high fidelity of the DeePTB-NEGF framework in simulating quantum transport in CNT-FETs, achieving DFT-level accuracy with TB efficiency. The framework accurately captures device physics across various nanotube diameters and channel lengths, showing excellent agreement with experimental data. This approach enables quantum transport analysis in realistic semiconductor devices and facilitates the optimization of future nanoelectronic device designs.

IV. SUMMARY AND DISCUSSION

In this work, we have developed DeePTB-NEGF, a deep learning-accelerated framework for efficient quantum transport simulations in nanoelectronic devices. This approach integrates deep learning (TB) Hamiltonian prediction with the NEGF method, enabling both direct quantum transport calculations and self-consistent solutions incorporating electrostatic effects. The framework achieves comprehensive simulation of dynamic break junction processes and CNT-FETs of experimental size under finite bias through NEGF-Poisson self-consistency.

The broad applicability and accuracy of this framework have been rigorously validated through the two representative applications. In break junction systems, we demonstrate the capability of our method to comprehensively simulate the junction evolution in both the metallic contacts and single-molecule junction. Our predicted conductance histograms show good agreement with experimental measurements in both cases, reproducing characteristic features such as the quantized conductance peaks between $1.0G_0$ and $2.0G_0$ for metallic contacts and the pronounced peak at $10^{-3.3}G_0$ for molecular junctions. Extending the framework to semiconduc-

tor devices, we simulated transfer characteristics of LBG CNT-FETs with dimensions matching experimental devices using the DeePTB-NEGF-Poisson implementation. Our simulations achieved excellent agreement with the measured transfer characteristic curve, highlighting both the efficiency and accuracy of our method and underscoring the importance of device-level simulations. Furthermore, the scaling potential of the LBG device geometry is explored with channel lengths ranging from 9 nm to 4 nm. Our simulations demonstrate that, without improvements in the geometry, the scaling potential remains limited.

Based on these achievements, the demonstrated performance of DeePTB-NEGF establishes a new paradigm for high-throughput quantum transport calculations in nanoelectronics. The framework's dual capability in simulating break junction processes and transistors in experimental size offers opportunities to advance both molecular electronics research and semiconductor device engineering. Further development of this methodology could incorporate more sophisticated quantum effects and extend to larger-scale systems, potentially enabling quantum transport simulations at industrially relevant scales.

The successful integration of deep learning efficiency with quantum mechanical accuracy presents a significant step toward bridging fundamental physics and technological applications in nanoelectronics.

V. DATA AVAILABILITY

VI. ACKNOWLEDGMENTS

[1] L. P. Kadanoff and G. Baym, *Quantum Statistical Mechanics: Green's Function Methods in Equilibrium and Non-Equilibrium Problems* (New York: W.A. Benjamin, 1962).

[2] L. V. Keldysh *et al.*, Diagram technique for nonequilibrium processes, Sov. Phys. JETP **20**, 1018 (1965).

[3] S. Datta, *Electronic Transport in Mesoscopic Systems* (Cambridge University Press, 1997).

[4] P. Hohenberg and W. Kohn, Inhomogeneous electron gas, Phys. Rev. **136**, B864 (1964).

[5] W. Kohn and L. J. Sham, Self-consistent equations including exchange and correlation effects, Phys. Rev. **140**, A1133 (1965).

[6] M. Brandbyge, J.-L. Mozos, P. Ordejón, J. Taylor, and K. Stokbro, Density-functional method for nonequilibrium electron transport, Phys. Rev. B **65**, 165401 (2002).

[7] E. Louis, J. A. Vergés, J. J. Palacios, A. J. Pérez-Jiménez, and E. SanFabián, Implementing the Keldysh formalism into *ab initio* methods for the calculation of quantum transport: Application to metallic nanocontacts, Phys. Rev. B **67**, 155321 (2003).

[8] E. Scheer and J. C. Cuevas, *Molecular electronics: an introduction to theory and experiment*, Vol. 15 (World Scientific, 2017).

[9] P. Gehring, J. M. Thijssen, and H. S. van der Zant, Single-molecule quantum-transport phenomena in break junctions, Nature Reviews Physics **1**, 381 (2019).

[10] M. Bürkle, U. Perera, F. Gimbert, H. Nakamura, M. Kawata, and Y. Asai, Deep-learning approach to first-principles transport simulations, Physical Review Letters **126**, 177701 (2021).

[11] R. Topolnicki, R. Kucharczyk, and W. Kaminski, Combining multiscale MD simulations and machine learning methods to study electronic transport in molecular junctions at finite temperatures, The Journal of Physical Chemistry C **125**, 19961 (2021).

[12] Q. Gu, Z. Zhouyin, S. K. Pandey, P. Zhang, L. Zhang, and W. E, Deep learning tight-binding approach for large-scale electronic simulations at finite temperatures with *ab initio* accuracy, Nature Communications **15**, 6772 (2024).

[13] Z. Zhouyin, Z. Gan, S. K. Pandey, L. Zhang, and Q. Gu, Learning local equivariant representations for quantum operators (2024), arXiv:2407.06053 [cond-mat.mtrl-sci].

[14] M.-M. Guo, Y. Jiang, J.-Y. Wang, Z.-N. Chen, S. Hou, and Q.-C. Zhang, Effectively enhancing the conductance of asymmetric molecular wires by aligning the energy level and symmetrizing the coupling, Langmuir **40**, 3759 (2024).

[15] A. D. Franklin, M. Luisier, S.-J. Han, G. Tulevski, C. M. Breslin, L. Gignac, M. S. Lundstrom, and W. Haensch, Sub-10 nm carbon nanotube transistor, Nano letters **12**, 758 (2012).

[16] N. Papior, N. Lorente, T. Frederiksen, A. García, and M. Brandbyge, Improvements on non-equilibrium and transport Green function techniques: The next-generation transiesta, Computer Physics Communications **212**, 8 (2017).

[17] A. Pecchia, G. Penazzi, L. Salvucci, and A. D. Carlo, Non-equilibrium green's functions in density functional tight binding: Method and applications, New Journal of Physics **10**, 065022 (2008).

[18] M. Klymenko, J. Vaitkus, J. Smith, and J. Cole, Nanonet: An extendable python framework for semi-empirical tight-binding models, Computer Physics Communications **259**, 107676 (2021).

[19] M. Anantram, M. S. Lundstrom, and D. E. Nikonov, Modeling of nanoscale devices, Proceedings of the IEEE

96, 1511 (2008).

[20] J. M. Soler, E. Artacho, J. D. Gale, A. García, J. Junquera, P. Ordejón, and D. Sánchez-Portal, The SIESTA method for *ab initio* order-n materials simulation, Journal of Physics: Condensed Matter **14**, 2745 (2002).

[21] B. Xu and N. J. Tao, Measurement of single-molecule resistance by repeated formation of molecular junctions, science **301**, 1221 (2003).

[22] Y. Yu, F. Cui, J. Sun, and P. Yang, Atomic structure of ultrathin gold nanowires, Nano letters **16**, 3078 (2016).

[23] L. Rego, A. Rocha, V. Rodrigues, and D. Ugarte, Role of structural evolution in the quantum conductance behavior of gold nanowires during stretching, Physical Review B **67**, 045412 (2003).

[24] C. M. Andolina, M. Bon, D. Passerone, and W. A. Saidi, Robust, multi-length-scale, machine learning potential for Ag–Au bimetallic alloys from clusters to bulk materials, The Journal of Physical Chemistry C **125**, 17438 (2021).

[25] M. J. Lagos, F. Sato, P. A. S. Autreto, D. S. Galvão, V. Rodrigues, and D. Ugarte, Temperature effects on the atomic arrangement and conductance of atomic-size gold nanowires generated by mechanical stretching, Nanotechnology **21**, 485702 (2010).

[26] T. N. Todorov and A. P. Sutton, Force and conductance jumps in atomic-scale metallic contacts, Phys. Rev. B **54**, R14234 (1996).

[27] T. P. Senftle, S. Hong, M. M. Islam, S. B. Kylasa, Y. Zheng, Y. K. Shin, C. Junkermeier, R. Engel-Herbert, M. J. Janik, H. M. Aktulga, *et al.*, The ReaxFF reactive force-field: development, applications and future directions, npj Computational Materials **2**, 1 (2016).

[28] C. Spearman, The proof and measurement of association between two things, The American journal of psychology **100**, 441 (1987).

[29] A. Sanchez-Soares, T. Kelly, G. Fagas, J. C. Greer, and E. Chen, Top-gated carbon nanotube fets from quantum simulations: Comparison with experiments, in *2021 International Symposium on VLSI Technology, Systems and Applications (VLSI-TSA)* (IEEE, 2021) pp. 1–2.

[30] J. Guo, A. Javey, H. Dai, and M. Lundstrom, Performance analysis and design optimization of near ballistic carbon nanotube field-effect transistors, in *IEDM Technical Digest. IEEE International Electron Devices Meeting, 2004.* (IEEE, 2004) pp. 703–706.

[31] S. Iijima, Helical microtubules of graphitic carbon, Nature **354**, 56 (1991).

[32] G. Pitner, Z. Zhang, Q. Lin, S.-K. Su, C. Gilardi, C. Kuo, H. Kashyap, T. Weiss, Z. Yu, T.-A. Chao, *et al.*, Sub-0.5 nm interfacial dielectric enables superior electrostatics: 65 mv/dec top-gated carbon nanotube fets at 15 nm gate length, in *2020 IEEE International Electron Devices Meeting (IEDM)* (IEEE, 2020) pp. 3–5.

[33] W. Cao, H. Bu, M. Vinet, M. Cao, S. Takagi, S. Hwang, T. Ghani, and K. Banerjee, The future transistors, Nature **620**, 501 (2023).

[34] L.-M. Peng, Z. Zhang, and S. Wang, Carbon nanotube electronics: recent advances, Materials today **17**, 433 (2014).

[35] H. K. Gummel, A self-consistent iterative scheme for one-dimensional steady state transistor calculations, IEEE Transactions on electron devices **11**, 455 (1964).

[36] G. Fiori, G. Iannaccone, and G. Klimeck, A three-dimensional simulation study of the performance of carbon nanotube field-effect transistors with doped reservoirs and realistic geometry, IEEE Transactions on electron devices **53**, 1782 (2006).

[37] P.-H. Ahn and S.-M. Hong, A fully coupled scheme for a self-consistent Poisson-NEGF solver, IEEE Transactions on Electron Devices **70**, 239 (2022).

[38] D. Marian, E. G. Marin, M. Perucchini, G. Iannaccone, and G. Fiori, Multi-scale simulations of two dimensional material based devices: the nanotcad vides suite, Journal of Computational Electronics **22**, 1327 (2023).

[39] K. Alam and R. Lake, Performance of 2 nm gate length carbon nanotube field-effect transistors with source/drain underlaps, Applied Physics Letters **87** (2005).

[40] J. Guo, S. Datta, and M. Lundstrom, A numerical study of scaling issues for schottky-barrier carbon nanotube transistors, IEEE transactions on electron devices **51**, 172 (2004).

[41] F. Leonard and D. A. Stewart, Properties of short channel ballistic carbon nanotube transistors with ohmic contacts, Nanotechnology **17**, 4699 (2006).

[42] L. Xu, J. Yang, C. Qiu, S. Liu, W. Zhou, Q. Li, B. Shi, J. Ma, C. Yang, J. Lu, *et al.*, Can carbon nanotube transistors be scaled down to the sub-5 nm gate length?, ACS Applied Materials & Interfaces **13**, 31957 (2021).

[43] A. Javey, J. Guo, Q. Wang, M. Lundstrom, and H. Dai, Ballistic carbon nanotube field-effect transistors, nature **424**, 654 (2003).

[44] F. Léonard and J. Tersoff, Multiple functionality in nanotube transistors, Physical review letters **88**, 258302 (2002).

[45] A. Pal, T. Chavan, J. Jabbour, W. Cao, and K. Banerjee, Three-dimensional transistors with two-dimensional semiconductors for future cmos scaling, Nature Electronics , 1 (2024).

[46] F. Pikus and K. Likharev, Nanoscale field-effect transistors: An ultimate size analysis, Applied Physics Letters **71**, 3661 (1997).